Atomic-Scale Structure of η-phase Mn$_3$N$_2$ (010) Studied by Scanning Tunneling Microscopy and First-Principles Theory

Haiqiang Yang, Rong Yang, and Arthur R. Smith[*]

Condensed Matter and Surface Science Program.Department of Physics and Astronomy, Ohio University, Athens, OH 45701

Walter R. L. Lambrecht

Department of Physics, Case Western Reserve University, Cleveland, OH 44106-7079

Abstract

The (010) surface of η-phase Mn$_3$N$_2$ grown on MgO(001) by molecular beam epitaxy is studied using scanning tunneling microscopy. The images show that the surface is composed of rows with spacing of 6.07 Å. Two types of domains with their c-planes perpendicular are observed in which the domain boundary is oriented at $\sim 45°$ to the c-planes. In other cases, the angle between the c-planes of the two domains is closer to 87°, consistent with a twin model in which the two domains meet along a (101) plane. Atomic resolution images vary with the sample bias. At lower sample bias, primarily Mn1 atoms are observed. At higher sample bias, both Mn1 and Mn2 atoms can be resolved. The dependence of the atomic resolution image on sample bias is explained by the ratio of the integrated local density of states of Mn1 to that of Mn2, which are based on first-principles theory. Simulations of the STM atomic-scale height profiles using the integrated local densities of states versus sample bias voltage are in excellent agreement with the experimental line profiles.

[*]Corresponding author, smitha2@ohio.edu

I. INTRODUCTION

Transition metal nitrides have recently drawn much attention due to their attractive physical properties, including structural, optical, electronic and magnetic properties, and their potential applications in various fields, including optical and wear-resistant coatings, magnetic recording and sensing, and spintronics.[1-10] Manganese nitride (Mn-N) is interesting due to its magnetic properties. It is known from previous bulk studies that manganese nitride has different bulk phases, including θ (MnN), η (Mn_3N_2), ε (Mn_4N), and ζ (Mn_5N_2, Mn_2N, and $Mn_2N_{0.86}$).[11-21] Both structural and magnetic measurements have been reported for most of these bulk phases, and particular attention has been paid to the θ-MnN, η-Mn_3N_2, and ε-Mn_4N. For the applications of this material, it is important to investigate the possibility of epitaxial growth. The control of the phases, and therefore the magnetic properties and orientations of manganese nitride grown on MgO(001) using molecular beam epitaxy (MBE), was reported by Yang et al recently.[7,8] The epitaxially grown phases can be controlled by the ratio of manganese to nitrogen and the substrate temperature. We have also recently investigated the surface magnetic structure of η-Mn_3N_2 (010) using atomic-scale spin-polarized scanning tunneling microscopy (SP-STM).[9]

In the present work, we discuss new results relating to the surface electronic structure of η-Mn_3N_2(010), presenting STM data acquired with normal (non-magnetic) STM tips. First, we present images of the sample surface in the vicinity of the boundaries which separate adjacent crystalline domains. Second, we present a detailed sample bias-dependent study of the structure of Mn_3N_2 (010), finding that the contrast behavior is consistent with expectations based on first-principles theory calculations.

II. EXPERIMENT

The experiments are performed in a custom-designed ultra-high vacuum system consisting of a MBE chamber coupled to a surface analysis chamber where the STM system is

located, which allow us to study the surfaces of grown films *in situ*. The MBE system includes a solid source effusion cell for Mn and a RF plasma source for N. After being heated up to 1000 °C for 30 minutes with the nitrogen plasma turned on, the MgO substrate temperature is lowered to the growth temperature of typically ~ 450°C (at this stage, the reflection high energy electron diffraction (RHEED) pattern of MgO is streaky, indicating the substrate is smooth after treatment), and the growth begins. The growth condition is monitored using RHEED which enables the determination of the surface crystal symmetry and surface lattice parameters. The growth rate is proportional to the measured Mn flux, which is $\text{Flux}_{Mn} = 3.2 \times 10^{14}$ cm^{-2}s^{-1}, resulting in a growth rate of ~ 35 Å/min; typical film thickness is ~ 2000-3000 Å.[8] The RHEED pattern of the Mn_3N_2 film is streaky, indicating epitaxial growth.[7,8] Following growth, the samples are investigated with *in situ* STM. For normal STM studies, we use electrochemically etched tungsten tips which are cleaned in the ultra high vacuum chamber using electron bombardment. All STM imaging is performed at ambient temperature (300 K) in constant current (CC) mode.

III. RESULTS AND DISCUSSION

A. Surface Domain Structure

The detailed bulk structure model for fct Mn_3N_2 has been discussed by Jacobs and Kreiner.[17,11] The Mn_3N_2 structure consists of a repetition of two layers of MnN followed by one layer of Mn where all Mn in the structure are located on the face-centered-tetragonal sub-lattice. This sequence repeats along the c-axis, and the lattice constants measured in our experiments are $a = b = 4.21$ Å, $c = 12.14$ Å.[8] Previously we have discussed the growth conditions leading to various different phases and orientations of Mn_xN_y. For Mn_3N_2, two orientations occur depending on Mn flux, one having c perpendicular to the growth surface and one having c in the plane of the growth surface.

Shown in Fig. 1(a) is a STM image of the surface of Mn_3N_2 (010) obtained at a sample

bias of -0.4 V and a tunneling current of 0.4 nA with a W tip. Clearly evident are row structures; their spacing is equal to $c/2$. A model of the Mn_3N_2 (010) face is displayed in Fig. 1(c). Two types of Mn atoms are distinguished as Mn1 and Mn2, with the former having only two N neighbors and the latter having three surface N neighbors and one second layer N neighbor. The observed rows correlate with the Mn1 rows of the model. The rows in the STM image cross over step edges without interruption or shift, indicating that the surface structure is directly correlated with the bulk structure.[7]

We see that there are two domains labeled by η-D1 and η-D2, respectively. Since the substrate [MgO(001)] has 4-fold symmetry, we expect equal quantities of both types of domains, and numerous domain boundaries (DBs) are commonly observed, as indicated by 'DB' in Fig. 1(a). The cause of the two types of domains is the 4% difference in lattice constant ($a = 4.21$ Å, while $c/3 = 4.047$ Å)[8] between the a and c axes of the fct Mn_3N_2 structure while the fcc (rock-salt) structure MgO substrate has 4-fold symmetry ($a_{MgO} = 4.213$ Å). Because of the two types of Mn_3N_2 domains which are present, the first-order diffraction streaks in the RHEED pattern appear to be split, as clearly seen in the cross-sectional line profile of the RHEED pattern taken along a [100] (simultaneously [001] direction) as seen in Fig. 1(b). The Mn_3N_2 line profile also shows one-third order streaks [$(\frac{1}{3},0)$, $(-\frac{1}{3},0)$, $(\frac{2}{3},0)$, $(-\frac{2}{3},0)$] which are caused by the triple layer periodicity along the [001] direction; their position corresponds to one-third of the spacing of the outer-most first-order streaks [$(1,0)$ and $(-1,0)$]. It can also be seen that the inner-most first-order Mn_3N_2 streaks coincide nearly perfectly with the first-order MgO streaks; the Mn_3N_2 lattice is matched very well to the substrate lattice along the a-axis.

We notice that the DB is typically at $\sim 45°$ to the row directions of both domains. This 45° angle is attributed to the need for the film to minimize interface mismatch between adjacent domains in the growing film. It can be understood simply in order to reduce bond strain at the planes where the domains meet. There are two in-plane Mn-N bond lengths, one is $a/2 = 2.105$ Å, the other is $c/6 = 2.024$ Å. If the domains came together along {100} or {001} planes, then the mismatch would be 4.0%. On the other hand, if the domains came

4

together along {101} planes, then the mismatch would be very small (or zero) since both unit cells have the same diagonal length. However, the [101] plane does not lie exactly at 45° with respect to the [100] plane or the [001] plane, but rather at about 46.13° and 43.87°, respectively. Therefore, if the adjacent domain rows are at exactly 90° to each other, this will lead to a divergent domain interface, as depicted in Fig. 2(a). A N atom at the upper right hand in the model is the starting point. As can clearly be seen, the 2.26° angular divergence leads to increasing spread of the two sides away from each other with increasing distance from the joining point. Boundary atoms in Fig. 2(a) are shown for each side. Pairs of these get further away from each other with distance along the interface. Presumably domain boundaries like this form when two adjacent domains nucleate at the MgO(001) surface but having their a-axes parallel to [100] and [010] *in-plane* surface directions of the substrate.

An ideal (101) interface would be possible only if the angle between rows of adjacent domains was 2.26° less than 90° which equals 87.74°, as depicted in Fig. 2(b). This boundary model corresponds in fact to a twin boundary. Twinning is very common in crystals, and here since the a and $c/3$ of Mn_3N_2 are only different by $\sim 4\%$, we would expect twinning to be common. In the twin boundary model of Fig. 2(b), the starting point is a N atom at lower left of the model. This interface model conserves many of the features of the normal Mn_3N_2 (010) surface. For example, at the (101) boundary, all Mn1 atoms (larger black dots) have just two N neighbors (tiny black dots) as usual at the surface (and in the bulk), whereas all Mn2 atoms (small gray dots) have four N neighbors (3 surface and one on the second layer) as usual. This rule is also followed at the region containing the skipped Mn1 row (see Fig. 2). Here, the interface boundary is about parallel to the Mn1 rows of domain D2 for a distance $3a$. We note from the STM image of Fig. 1(a) that the regions between Mn1 atom rows, containing Mn2 and N atoms, appear as the valleys or trenches. The skipped rows in the image appear to have a trench running completely around their ends. This is provided for in the model of Fig. 2(b) where Mn2 and N atoms clearly separate the skipped Mn1 row from the surrounding Mn1 rows.

To determine precisely the angle between the rows (c-planes) in two adjacent domains, careful image correction is necessary. The first step of this procedure is to correct for thermal drift using two consecutive images, one acquired bottom to top, the other top to bottom. Second, a stretch by a fixed (known) percentage is applied along the y-direction to correct for x-y scanner asymmetry. In the case of the image of Fig. 1(a), we find after correction that the row spacing ($c/2$) in both domains agrees to within 1%, as we would expect. This is indicated by the thick bars in each domain which each have the same length, are perpendicular to their respective rows, and cross an equal number of rows. However, the measured angle between the rows (c-planes) of the adjacent domains is only $\sim 87°$. This is clearly consistent with the twinning model shown in Fig. 2(b), suggesting that twinning is occuring, most likely at the nucleation stage, resulting in ideal (101) twinned domain boundaries. We expect that one of the two twins would have one a-axis in registry with the MgO lattice, while the other would be rotated a few degrees away from the substrate symmetry direction.

After carefully measuring a number of STM images, it is found that not all domain boundaries have their angles between the rows less than 90°. An example is shown in Fig. 3. For this image, after correction for drift and scanner asymmetry, the row spacing is found to be equal on both sides of the domain boundary, as indicated by the thick lines which are equal in length, perpendicular to their respective rows, and crossing an equal number of rows; but in addition, the rows from the adjacent domains are at very close to 90° to each other. This suggests that the two domains are not twins, and that their (101) planes do not coincide. This results in a divergence, as the model of Fig. 2(a) suggests. Of course the rows may extend to prevent the divergence, which requires a more complicated model. We also note the existence of a dislocation in the domain on the right hand side in which the rows are shifted by about half of $c/2$. This dislocation is likely caused by the domain mismatch-induced stress rather than cooling-induced stress (growth temperature is $\sim 450°C$) since it does not extend across the domain boundary. Another possibility is that since the film has $3\times$ the periodicity of the substrate, the dislocation could also be an anti-phase domain

6

boundary due to two different Mn_3N_2 nuclei growing and colliding, in much the same way the other domain boundaries formed. We also note an apparent dip (dark area) near the boundary at the point where the dislocation intersects the boundary; this apparent dip is attributed to the domain interface divergence.

Some other interesting features seen in the image of Fig. 1(a), which are evident at the domain boundaries, are marked in the image. Skipped rows are very common. At certain places along the domain boundary where the rows converge, a row in one domain continues past two rows in the adjacent domain, and it then converges with the next row. Thus one row is skipped at the domain boundary. Sometimes two or even three rows are skipped. This skipping behavior could also be viewed as the domain boundary exhibiting (100) facets.

To visualize how much a skipped row would possibly affect the divergence of two domains, we construct identical loops around a normal part (loop A) of the diverging interface model of Fig. 2 and also around a part of the diverging interface containing a skipped row (loop B). We add up the vector distances along each loop, arriving at an offset vector for each. For the diverging model of Fig. 2(a), each loop shows about the same offset vector. Thus the skipped row does not solve the divergence problem.

We construct similar loops in the case of the twin boundary model of Fig. 2(b). For loop A there is no offset vector, while for loop B, we see a tiny offset vector due to the skipped row. Thus in case of twinning, a skipped row should cause a small amount of strain.

Further interface defects are found in the images. An example is shown in Fig. 1(a) at the upper right part of the domain boundary where it crosses the step. A box is placed across the interface such that two corners coincide with the domain boundary. There are 15 rows entering the box (including at the box edge) on the left side of the interface, while there are only 12 rows exiting the box on the right side of the interface. The box includes one skipped row on the left side, which accounts for two extra rows on the left compared to the right side. However, it still leaves one extra row entering on the left side which does not exit on the right side.

B. Bias-Dependent Atomic-Scale Surface Structure

1. Experiment

With a sufficiently sharp STM tip, atomic resolution images of this surface can be obtained. Shown in Fig. 4 are the sample bias dependent images of the Mn_3N_2 (010) surface at atomic resolution. In these images, both Mn1 and Mn2 atoms are observed with varying resolution depending on the bias. In all of the images, the brightest dots (labeled with ×'s) correspond to the Mn1 atoms which have only two bonds to the neighboring N atoms in the surface layer. The vertical rows of Mn1 atoms also correspond to the middles of the rows seen at lower resolution in Figs. 1 and 3. The Mn2 atoms are the other less bright dots (labeled with ○'s) seen in Fig. 4. The atomic resolution images have an exact correspondence with the face-centered tetragonal, bulk-terminated (010) surface model shown in Fig. 1(c). Since over the whole range of positive and negative sample bias, any given atom appears as a protrusion in both filled and empty states, and also since we are able to acquire images down to very small voltages (0.2 V or even smaller), we know that the surface is metallic. The metallic behavior can also be observed from the plot of the theoretical ILDOS about the Fermi level, as plotted in Fig. 5(a), which indicates the existence of states at the Fermi level; a thorough discussion of the electronic structure of MnN and Mn_3N_2 has been performed by Lambrecht *et al.*, which finds that these systems are metallic.[26]

As the sample bias voltage varies between +0.8 V and -0.4 V, we do observe a variation of the contrast such that Mn1 and Mn2 are of about the same brightness at larger magnitudes of sample bias voltage, whereas Mn1 dominates over Mn2 at smaller magnitudes of sample bias voltage. In particular, the atoms Mn1 and Mn2 are both clearly resolved at positive sample biases $V_S \geq 0.6$ V and at negative sample biases $V_S \leq$ -0.3 V, but for sample biases within the range +0.5 V $\geq V_S \geq$ -0.2 V, the atom Mn1 appears brighter and the atom Mn2 appears less bright. This bias dependence is somewhat unexpected, since for a metallic surface, it is often thought that the best atomic resolution should be obtained at the lower

bias voltages where the tip is closer to the surface and that the resolution decreases with increasing voltage. However, this is not the case with Mn_3N_2 (010).

2. Comparison of Experiment with Theory

To explain the observed behavior, we consider that the tunneling current above a given surface location is going to depend on the local density of states (LDOS) at that position. According to STM theory, we may write the tunneling current I_t as:

$$I_t \sim n_T \int_{E_F}^{E_F+V} n_S(\vec{R}_t, E)dE \tag{1}$$

where E_F is the Fermi level of the sample, n_T is the local density of states of the tip (assumed constant over the range of integration), and $n_S(\vec{R}_t, E)$ is the LDOS of the sample at energy E and tip position $\vec{R}_t$. Therefore, the tunneling current is proportional to the integrated LDOS (ILDOS) of the sample, $\tilde{n}_S(\vec{R}_t)$. The larger the $\tilde{n}_S(\vec{R}_t)$ is, the larger the tunneling current will be and the brighter a given surface feature will appear in constant current mode. Of course, when the $\tilde{n}_S$ for Mn1 and Mn2 are equal at a certain energy, then we may still observe a height difference between the two due to geometrical relaxation.

To obtain the LDOS for Mn_3N_2, we employ theoretical calculations using the full-potential linear muffin-tin orbital method[22] in the local spin density functional approximation[23,24]. The main results of these calculations and details of the approach are presented elsewhere[25,26]. The calculations result in the partial DOS for both Mn1 and Mn2 separately, as well as for N. For purposes of application to STM simulations, we only take into account the partial DOS due to the Mn atoms. This is justified based on the recent work of Lambrecht *et al.* which shows that in MnN the predominantly N bands, or more precisely, the N_{2p}-Mn_d bonding bands occur betweem -2.5 eV and -7.5 eV below the Fermi energy. While the N contribution to the LDOS is not zero near the Fermi energy, it is much smaller than the Mn contribution (by a factor of at least 5). The same is true for Mn_3N_2 (although not shown explicitly in that paper).

Shown in Fig. 5(a) is a plot of the ILDOS of Mn1 ($\tilde{n}_{Mn1}$) and Mn2 ($\tilde{n}_{Mn2}$) over the range -0.6 eV to + 0.8 eV, negative energy corresponding to filled states and positive energy to empty states. The integral of the LDOS starts at energy = 0 and extends to both positive and negative energies. The STM tunneling current when the tip is directly above a Mn1 atom should be proportional to $\tilde{n}_{Mn1}$. The STM tunneling current when the tip is directly above a Mn2 atom should be proportional to $\tilde{n}_{Mn2}$.

To compare these theoretical ILDOS values with the actual STM data of Fig. 4, it is most useful to compute the ratio $R = \tilde{n}_{Mn1}/\tilde{n}_{Mn2}$. This ratio is shown in Fig. 5(b) as a function of energy. As can be seen, R is largest (R=1.35) at V_S = -0.1 V and drops off with increase of the magnitude of the energy on either side. We also observe that it is asymmetric with respect to the Fermi level. On the negative sample bias side, R drops quickly with the increase of the magnitude of the voltage reaching $R = 1.15$ at V_S = -0.4 eV, whereas on the positive side, R decreases slowly over the range 0.0 V < V_S ≤ ~ +0.4 eV reaching $R = 1.28$, then drops quickly over the range +0.4 V ≤ V_S ≤ +0.8 eV reaching $R = 0.9$.

Comparison of the STM data of Fig. 4 with the calculation in Fig. 5 clearly shows that the ratio R is in general directly related to the resolution of Mn1 and Mn2 atoms. For both bias polarities, when $R > 1.2$, Mn1 dominates Mn2 in the STM image; when $R < 1.2$, both atoms Mn1 and Mn2 are clearly resolved. The decrease of R with increasing negative voltage leads to both Mn1 and Mn2 being clearly resolved at V_S = -0.3 V, whereas the slower decrease of R with increasing positive voltage up to +0.4 V leads to Mn1 and Mn2 being both clearly resolved for V_S ≥ 0.6 V. Thus, we find that the resolution of atoms Mn1 and Mn2 observed in the experiment is qualitatively well explained using the results of the ILDOS calculations. We note that $R = 1.0$ in the range +0.6 V < V_S < +0.7 V. The height difference between Mn1 and Mn2 in this range is about 0.08 Å, which is attributed to geometrical relaxation of the surface atoms.

3. Quantitative Comparison via STM Line Profile Simulation

Quantitative comparisons between the STM images and first-principles calculations can be done by taking line profiles of the STM image data and comparing those with line profile simulations based on the ILDOS calculations. In order to observe directly the contrast between Mn1 and Mn2, it is useful to take the line profiles along the [101] direction cutting across both Mn1 and Mn2, as indicated in Fig. 4(a). To compare the experimental CC mode height profiles with theory, simulated CC height profiles $z(x,V)$ are obtained by simulating the tunneling current I_t with an exponentially weighted sum over surface atoms, as

$$I_t \sim \sum n_T \tilde{n}_S(\mathbf{R}_i) e^{-2\kappa |\mathbf{R}_T - \mathbf{R}_i|}. \tag{2}$$

where $\kappa = 1.14$ $\mathring{A}^{-1}$, corresponding to a work function of 5 eV.[27] In Fig 6(a) is shown the surface cell over which the sum in Eq. 2 is performed; the cell size is sufficient to provide convergence of the sum. To obtain the simulated profile, the lateral position x of the tip is varied along the direction of the dashed line shown in Fig. 6(a). At each position x of the tip, the sum over atoms shown in Fig. 6(a) is performed according to Eq. 2, using $\tilde{n}_{Mn1}$ and $\tilde{n}_{Mn2}$ for the ILDOS of Mn1 and Mn2, respectively [shown in Fig. 5(a)]. The absolute tip-sample distance $z(x,V)$, defined as the vertical position z_{tip} of the nucleus of the tip apex atom relative to the vertical position of the nucleus of the Mn1 atoms z_{Mn1}, is determined from Eq. 2 in order to obtain a constant current I_t at each position x. The simulated CC height profile $z(x,V)$ is then obtained for a given voltage V_S. The simulated STM corrugation profile is then equal to the simulated CC height profile minus a constant. For comparison with the STM data, it is sufficient to simulate a single unit cell and repeat as necessary.

Fig. 6(b) shows the simulated height $z(x_{Mn1},V)$ of the tip at the position x_{Mn1} directly above the Mn1 atoms as a function of the sample bias voltage V_S. The proportionality constant between I_t and the sum in Eq. 2 was chosen so that $z(x_{Mn1},+0.2 \text{ V}) = 4.00$ Å. Typical values for absolute tip-sample distances are in the range 3-7 Å.[28,29]It is seen from

Fig. 6(b) that the tip-sample distance is smallest at low bias voltage and larger at higher bias voltage.

We have also performed constant height (CH) current profile simulations using a very similar procedure. In this case, the tip height z(V) is held constant at each position x of the tip and depends only on the bias voltage. In this case z(V) is very similar to that shown in Fig. 6(b). The sum in Eq. 2 is then performed at each position x, again using $\tilde{n}_{Mn1}$ and $\tilde{n}_{Mn2}$ for the ILDOS of Mn1 and Mn2, obtaining a value proportional to the tunneling current I_t(x,V). A plot of I_t(x,V) then corresponds to the CH current profile simulation. We find that the CC height profile simulation and the CH current profile simulation are very similar at any given bias voltage.

The experimental height profiles along the [101] direction cutting across Mn1 and Mn2 atoms are obtained from the STM images as a function of sample bias voltage and displayed in Fig. 7(a). Each height profile shows five high Mn1 peaks corresponding to the Mn1 atoms, and each Mn1 peak has a lower Mn2 peak or shoulder on each side corresponding to the Mn2 atoms. One can see that the average total corrugation is maximum at $V_S = +0.2$ V and that it gets smaller with increasing positive or negative voltage. This total corrugation amplitude $A_{Mn1,exp}$ is displayed in Fig. 8(a) as a function of V_S. Also, one can see that at $V_S = +0.8$ V and -0.4 V, the height difference between the Mn1 and Mn2 peaks is less than at +0.2 V or -0.2 V. The experimental peak amplitude ratio $R_{P,exp} = A_{Mn1,exp}/A_{Mn2,exp}$, where $A_{Mn2,exp}$ is the corrugation amplitude of Mn2 atoms, is displayed in Fig. 8(b) as a function of V_S. Clearly, $R_{P,exp}$ is maximum at small voltage, where $\tilde{n}_{Mn1}/\tilde{n}_{Mn2}$ is larger, whereas $R_{P,exp}$ gets smaller at larger magnitude of voltage, where $\tilde{n}_{Mn1}/\tilde{n}_{Mn2}$ is smaller (see Fig. 5).

Fig. 7(b) shows the simulated CC corrugation profiles which have each been multiplied by a normalization constant = 3 such that the total simulation corrugation amplitude $A_{Mn1,sim}$ at V(S) = +0.2 V is matched to the STM data at +0.2V. Also note that the minimum of each corrugation profile has been set to zero. At V(S) = +0.8V, one can see clearly both the Mn1 and Mn2 peaks corresponding to the Mn1 and Mn2 atoms, respectively. This

simulation compares very well with the experimental data (shown to its left), although $A_{Mn1,sim}$ is about half of $A_{Mn1,exp}$. For the sample bias voltage of +0.7 V, $A_{Mn1,sim}$ is larger, again consistent with the experiment, and the Mn2 peaks are still apparent. For yet smaller positive biases, $A_{Mn1,sim}$ continues to increase, reaching its maximum at +0.2 V, where the Mn2 appear only as shoulders; then $A_{Mn1,sim}$ is decreased very slightly at -0.2 V and further decreased at -0.4 V where Mn2 appears more clearly. The simulated amplitude $A_{Mn1,sim}$ is plotted together with $A_{Mn1,exp}$ in Fig. 8(a), where reasonable agreement is found overall. Furthermore, the simulated amplitude ratio $R_{P,sim} = A_{Mn1,sim}/A_{Mn2,sim}$ is plotted together with the experimental one, $R_{P,exp}$, in Fig. 8(b). Overall, the simulated and experimental bias-dependent ratios follow the same trend very closely.

The actual experimental STM height profiles shows small peaks at the Mn2 positions at all bias voltages, whereas the simulated profiles show Mn2 peaks at only the largest magnitudes of bias voltage. This discrepancy may be due to our neglect of the directional character of the d-orbitals in the simulation based on Eq. 2 which assumes a spherical wave function shape. The orbitals of the Mn and W tip involved are in reality d-orbitals and would require a more involved simulation. Furthermore, the fact that the simulated corrugation amplitudes (before normalization) are on average about 33% of the experimental corrugation amplitudes is also consistent with the well-known fact that such atom superposition simulations do not achieve the corrugations found in experiment.[28,30]

The results show that when the tip-sample spacing is small at low bias voltage, the magnitude of the corrugation is large; however, the corrugation of Mn1 is dominant due to the ILDOS of Mn1 dominating that of Mn2. When the bias voltage increases, the tip-sample distance increases, resulting in the decrease of the overall corrugation amplitude; however, the corrugations of Mn1 and Mn2 then become more similar since the ILDOS values for Mn1 and Mn2 have smaller relative difference. Simulation and experiment give a consistent picture; the ILDOS can be used to explain the STM data quite well.

IV. CONCLUSIONS

In conclusion, the (010) surface of η-phase Mn_3N_2 grown by MBE is studied by STM. The STM images show that the surface is composed of row structures with row spacing of $\sim$ 6.07 Å. The rows from different domains meet at the domain boundary in some cases at 90° where two domains are joined, but in other cases at $\sim$ 87°, consistent with a twinned domain boundary. The domain boundaries commonly appear at $\sim$ 43-45° to the row directions. Such interfaces provide the best lattice matching between domains. Skipped rows at the domain boundary are common but do not appear to influence strain greatly.

The change of the atomic resolution images with sample bias is understood by the change of the ratio of the ILDOS of Mn1 to that of Mn2. Mn1 dominates Mn2 in the image for small magnitude of sample bias due to large Mn1:Mn2 ILDOS ratio, whereas both Mn1 and Mn2 are resolved clearly at large magnitude of sample bias due to smaller Mn1:Mn2 ILDOS ratio. Simulation of the STM image CC height profiles using ILDOS values based on first-principles theory finds excellent agreement with the experimental CC height profiles as a function of sample bias, after normalization of the corrugation amplitudes. These results show that STM height profile, atom-superposition simulations based on simple s-like exponential decay of the wave function into the vacuum work quite well. However, to obtain the correct absolute corrugation amplitudes, one likely would need to consider d-orbitals. Lastly, we note that the Mn_3N_2 (010) surface is a relaxed, bulk-like surface, similar to the case of rocksalt ScN, and because of the Mn having spin and also because of the 3× superstructure, this surface is ideal for testing theories of spin-polarized STM.[9,31]

V. ACKNOWLEDGEMENTS

REFERENCES

[1] J. P. Dismukes, W. M. Yim, and V. S. Ban, J. Cryst. Growth **13/14**, 365 (1972).

[2] T. D. Moustakas, R. J. Molnar, and J. P. Dismukes, Electrochem. Soc. Proceedings **96-11**, 197 (1996).

[3] D. Gall, I. Petrov. P. Desjardins, and J. E. Greene, J. Appl. Phys. **86**, 5524 (1999).

[4] D. Gall, I. Petrov, N. Hellgren, L. Hultman, J. E. Sundgren, and J. E. Greene, J. Appl. Phys. **84(11)**,6034 (1998).

[5] H. A. H. Al-Brithen, A. R. Smith, Appl. Phys. Lett. **77**, 2485(2000).

[6] A. R. Smith, H. A. H. Al-Brithen, D. C. Ingram, and D. Gall, J. Appl. Phys. **90**, 1809 (2001).

[7] H.Q. Yang, H. Al-Brithen, A.R. Smith, J. A. Borchers, R. L. Cappelletti, M. D. Vaudin, Appl. Phys. Lett. **78**, 3860 (2001).

[8] H.Q. Yang, H. Al-Brithen, A.R. Smith, E. Trifan, and D. C. Ingram, J.Appl. Phys. **91, 1053 (2002)**.

[9] H.Q. Yang, A.R. Smith, M. Prikhodko, W.R.L. Lanbrecht, Phys. Rev. Lett. **89, 226101 (2002).**

[10] S Yang, D.B. Lewis, I. Wadsworth, J. Cawley, J.S. Brooks, and W.D. Munz, Surf. and Coat. Technol. **131**, 228 (2000); K. Inumaru, T. Ohara, and S. Yamanaka, Appl. Surf. Sci. **158**, 375 (2000).

[11] G. Kreiner, and H. Jacobs, J. Alloys and compounds **183**, 345 (1992).

[12] K. Suzuki, T. Kaneko, H. Yoshida, Y. Obi, H. Fujimori, H. Morita, J. Alloys and Compounds **306**, 66 (2000).

[13] F. Lihl, P.Ettmayer, A. Kutzelnigg, Z. Metallk. **53**, 715 (1962).

16

[14] N. Otsuka, Y. Hanawa, and S. Nagakura, Phys. Stat. Sol. (a), **43**, K127 (1977).

[15] M. Tabuchi, M. Takahashi, and F. Kanamaru, J. Alloys and Compounds **210:(1-2)**, 143 (1994).

[16] A. Leineweber, R. Niewa, H. Jacobs, and W. Kockelmann, J. Materials Chemistry **10:(12)**, 2827 (2000).

[17] H. Jacobs and C Stuve, J. Less Common Metals, **96**, 323, (1984).

[18] G.W. Wiener, J.A. Berger, J. Met., **7**, 360 (1955).

[19] W.J. Takei, R. R. Heikes, and G. Shirane, Phys. Rev. **125**, 1893 (1962).

[20] M. Mekata, J. Phys. Soc. Jpn., **17**, 796 (1962).

[21] M. Mekata, J.Haruna, H. Takei, J. Phys. Soc. Jpn., **25**, 234 (1968).

[22] M. Methfessel, M. van Schilfgaarde and R. A. Casali, in Electronic Structure and Physical Properties of Solids: The Uses of the LMTO Method, edited by Hugues Dreyss'e, Lecture Notes in Physics, (Springer, Berlin 2000), p.114-147.

[23] W. Kohn and L. J. Sham, Phys. Rev. **140**, A1133(1965).

[24] U. von Barth and L. Hedin, J. Phys. **C5**, 2064(1972).

[25] M.Prikhodko, W.R.L. Lambrecht, Bull. Am. Phys. Soc. **47**, M19.005(2002).

[26] W. R. L. Lambrecht, M. prikhodko and M. S. Miao, Phys. Rev. B (in press).

[27] Note: we have also tried smaller work functions such as 3 eV in our simulations, with similar results.

[28] C. J. Chen, Introduction to Scanning Tunneling Microscopy, Oxford University Press, p. 38 (1993).

[29] We have also tried our simulations with slightly larger tip-sample spacing of 4.5 Å, which

changes the simulation very little except that the corrugations get smaller by about 11%.

[30] S. Heinze, S. Blügel, R. Pascal, M. Bode, and R. Wiesendanger, Phys. Rev. B **58(24)**, 16432 (1998).

[31] D. Wortmann, S. Heinze, Ph. Kurz, G. Bihlmayer, and S. Blügel, Phys. Rev. Lett. **86**, 4132 (2001).

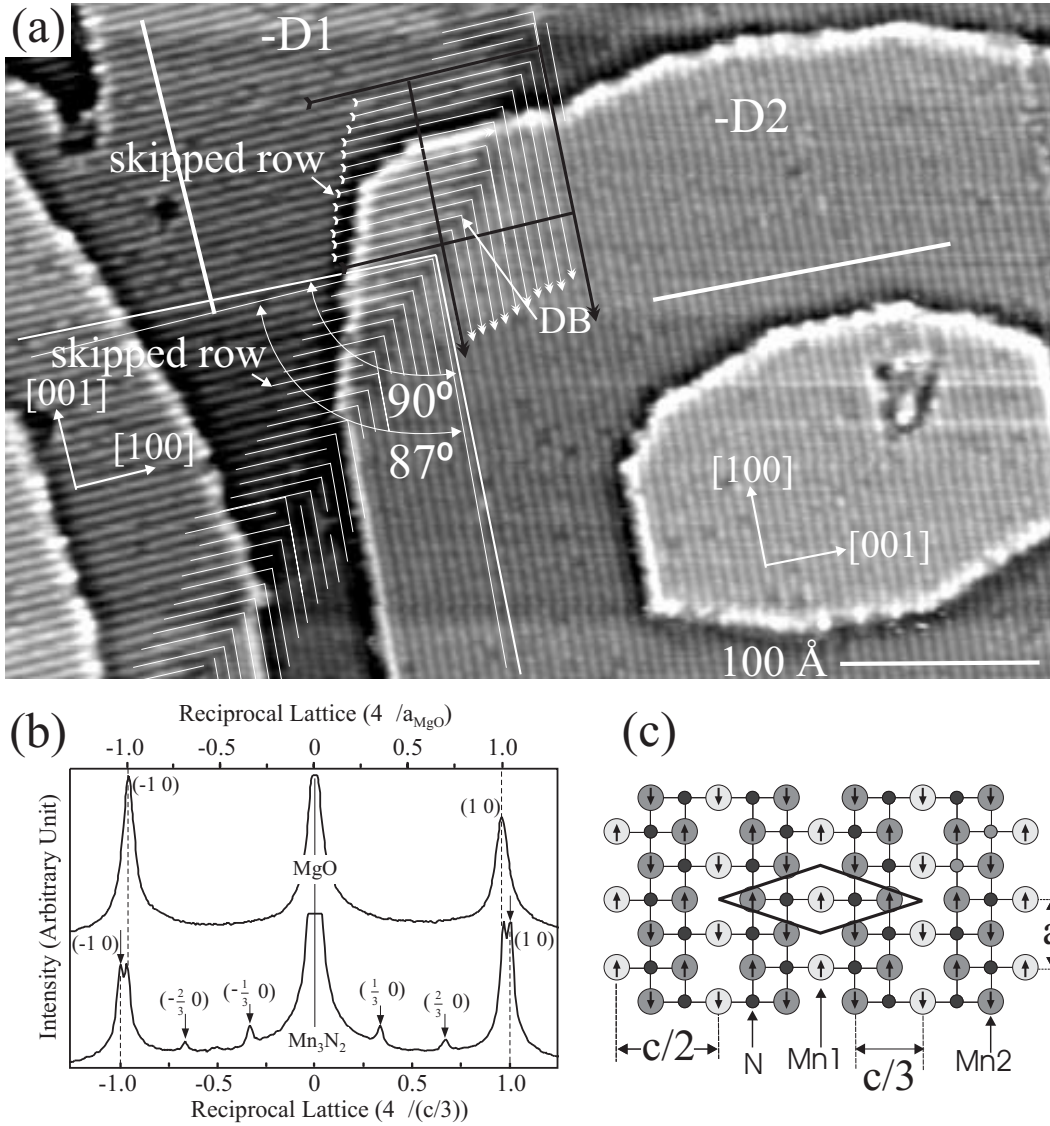FIG. 1. (a) STM image of the (010) surface of Mn_3N_2 obtained at a sample bias of -0.4 V and a tunneling current of 0.4 nA. η-D1 and η-D2 indicate two types of domains of η-phase Mn_3N_2. Corner angles indicate the domain boundary. Wide lines perpendicular to the rows in each domain are of equal length and contain an equal number of rows. The image is displayed with a local background subtraction to allow viewing of all terraces. Minimum step height is $b/2$, and row height corrugation is $\sim 0.xx$ Å; (b) line profile of the RHEED pattern of the surface; (c) bulk-terminated surface model of Mn_3N_2 (010). The arrows in the shaded circles show the orientations of the spins of the Mn atoms. The rhombus indicates the non-magnetic unit cell of the surface.

(a) Divergent Domains at 90

D1

B

skipped row →

90

A

D2

Mn1   Mn2   N

(b) Twinned Domains at 87.74

D1

B

87.74

A

D2

Mn1   Mn2   N
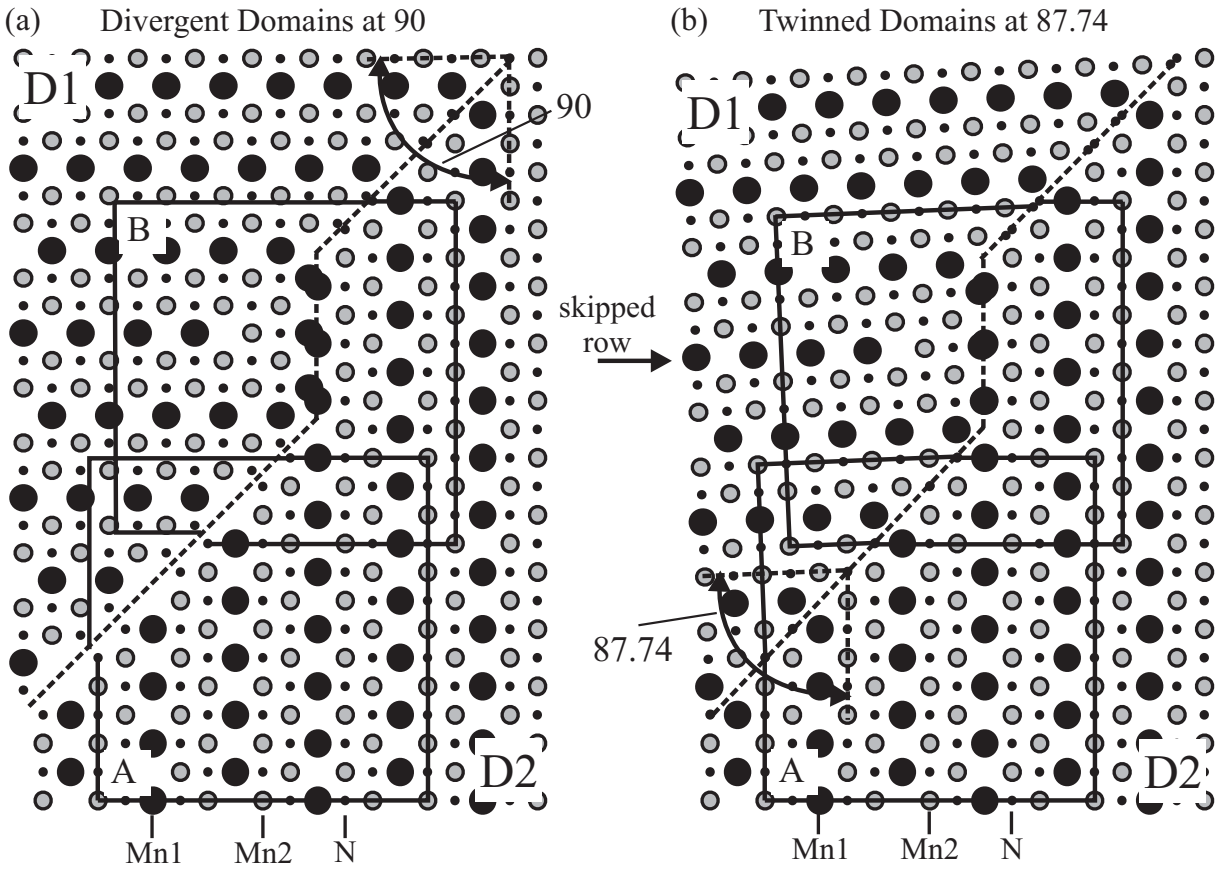
FIG. 2. Mn_3N_2 (010) surface models in the vicinity of a domain boundary and a skipped row. (a) diverging model with domain rows at 90°; (b) twin model with domain rows meeting at 87.74°.
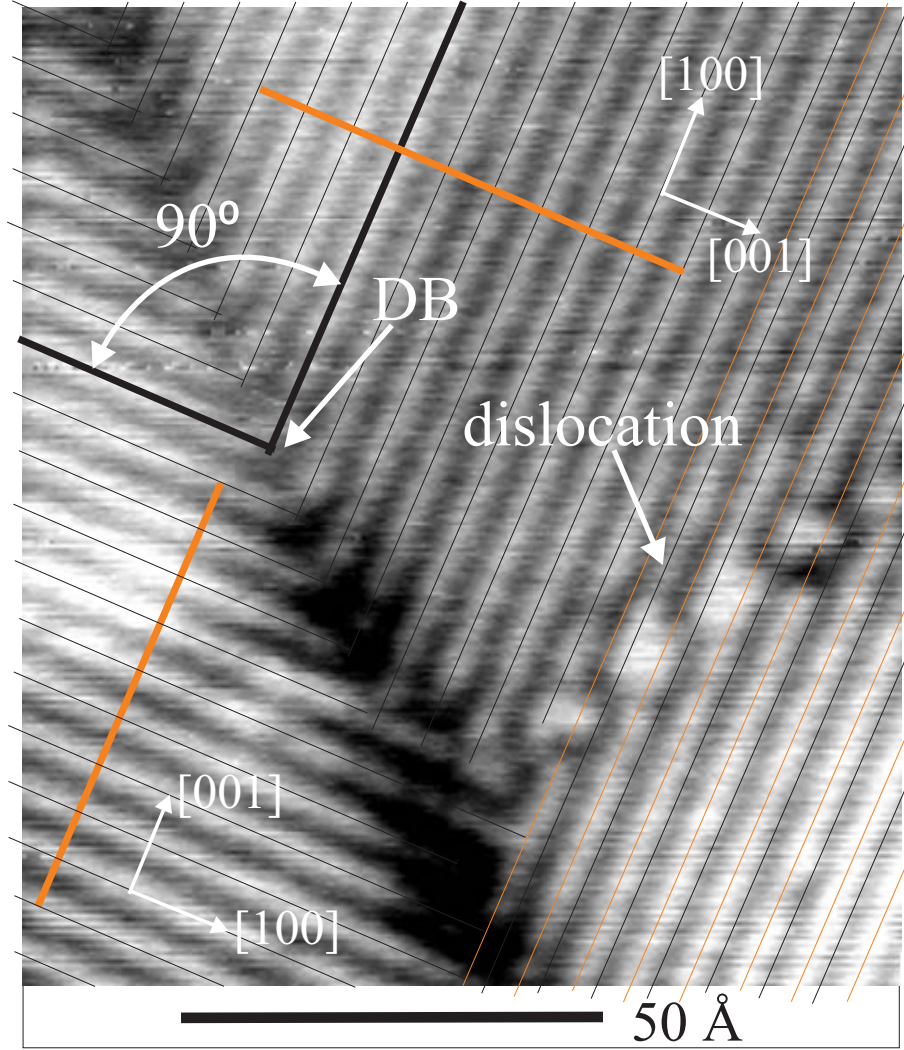
FIG. 3. STM image of Mn_3N_2 (010) domain boundary region obtained at a sample bias of -0.1 V and tunneling current of 0.8 nA. Wide bars in each domain are of same length and contain an equal number of rows. Domains meet at 90°. Narrow lines fit to the rows show the shift due to the dislocation.
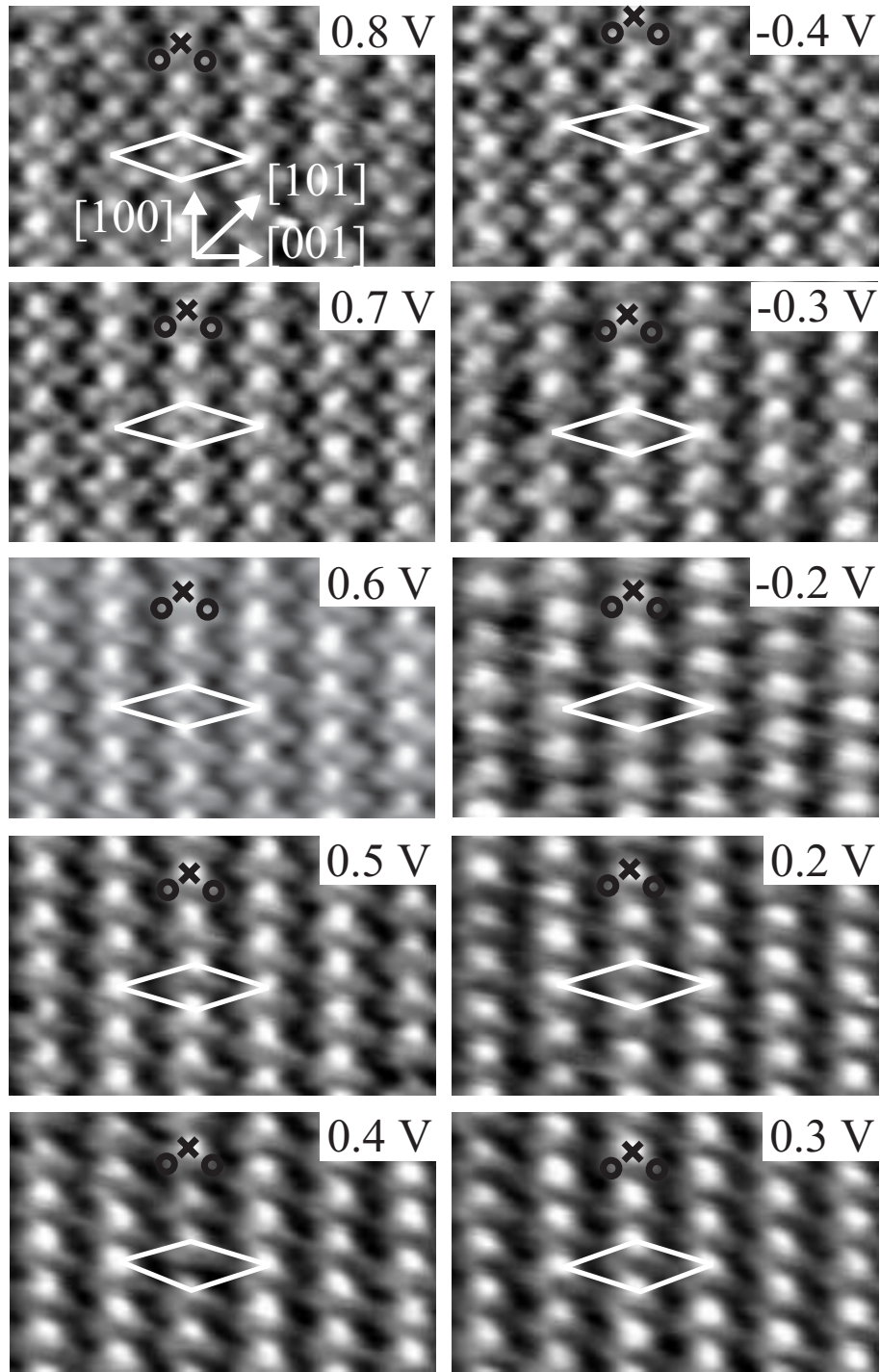
FIG. 4. Bias dependent STM images acquired with a tunneling current of 0.4 nA. Rhombus shows the unit cell of the surface. The ×'s correspond to the Mn1 atoms, while the ∘'s correspond to the Mn2 atoms.
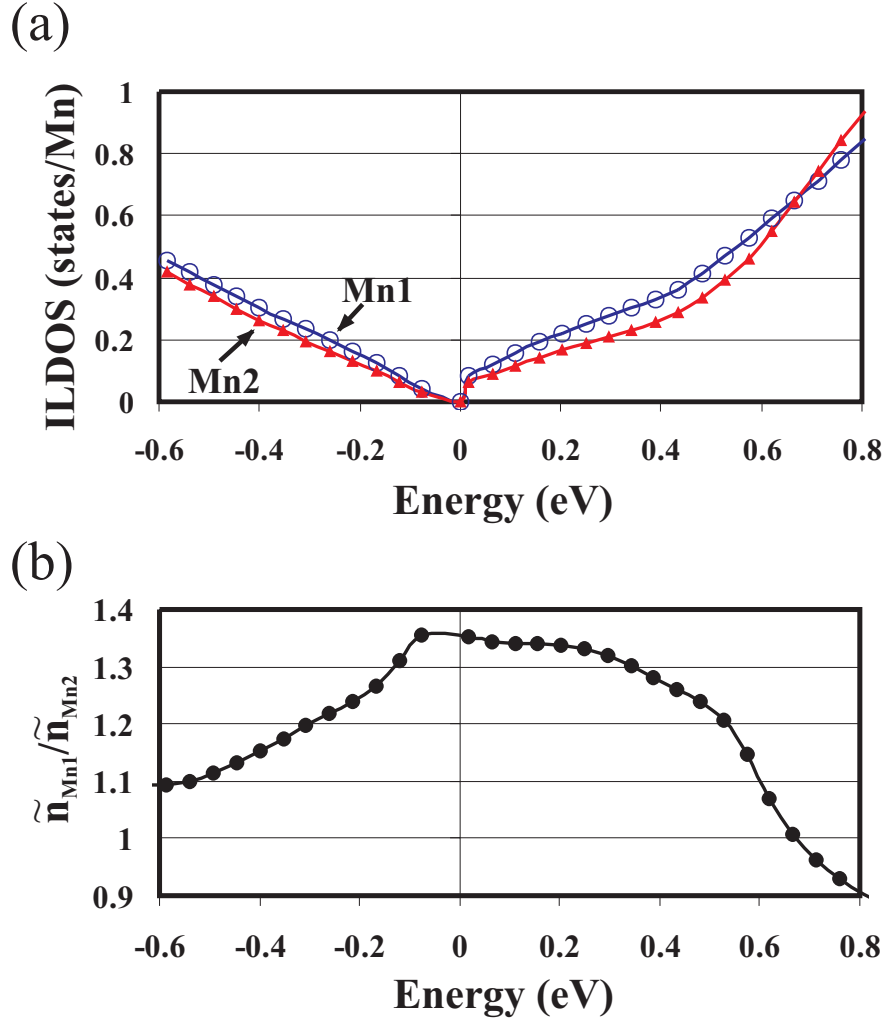
FIG. 5. (a) Plot of the ILDOS of Mn1 and Mn2 vs. energy relative to the Fermi level at 0 eV (Mn1 circles; Mn2 triangles); (b) plot of the ratio of ILDOS of Mn1 to that of Mn2 vs. energy. Mn1 dominates the STM image for ratios above the dashed line.
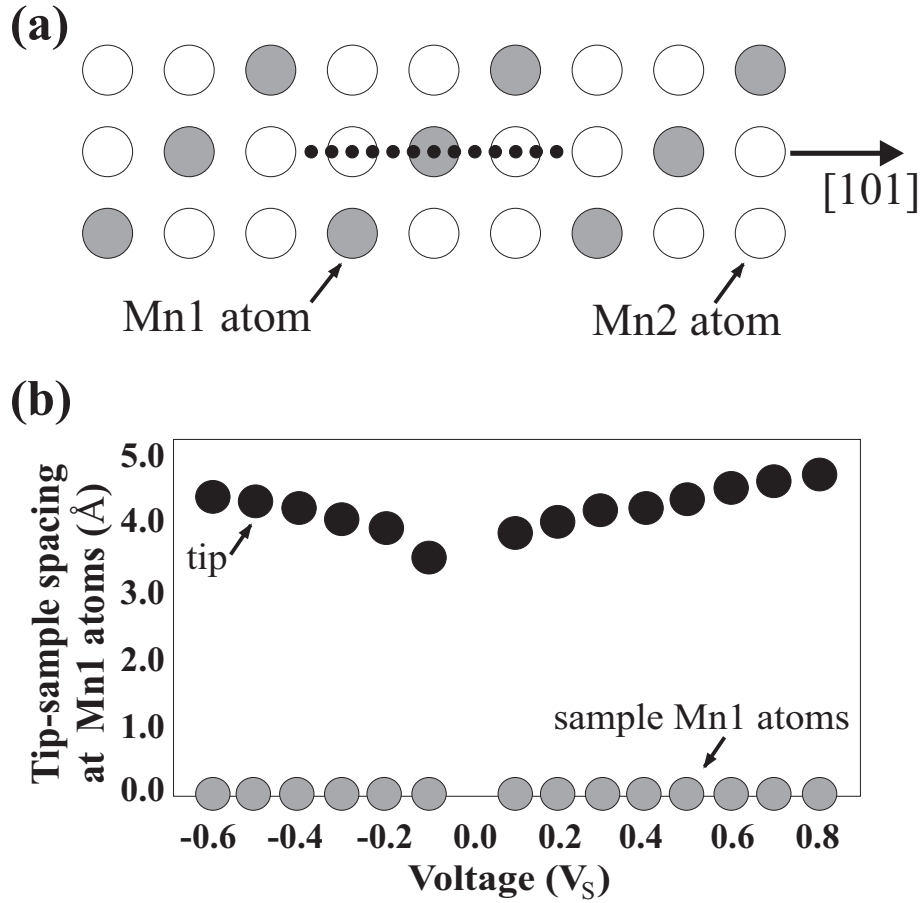
(a)

Mn1 atom Mn2 atom [101]

(b)

FIG. 6. (a) Surface cell used to perform the height profile simulations. Mn1 and Mn2 atoms are indicated. Small solid dots indicate the positions of the STM tip used to obtain one unit cell of the line profile. (b) Plot of the tip-sample distance at the position of the Mn1 atoms as a function of bias voltage, determined from the CC height profile simulations.
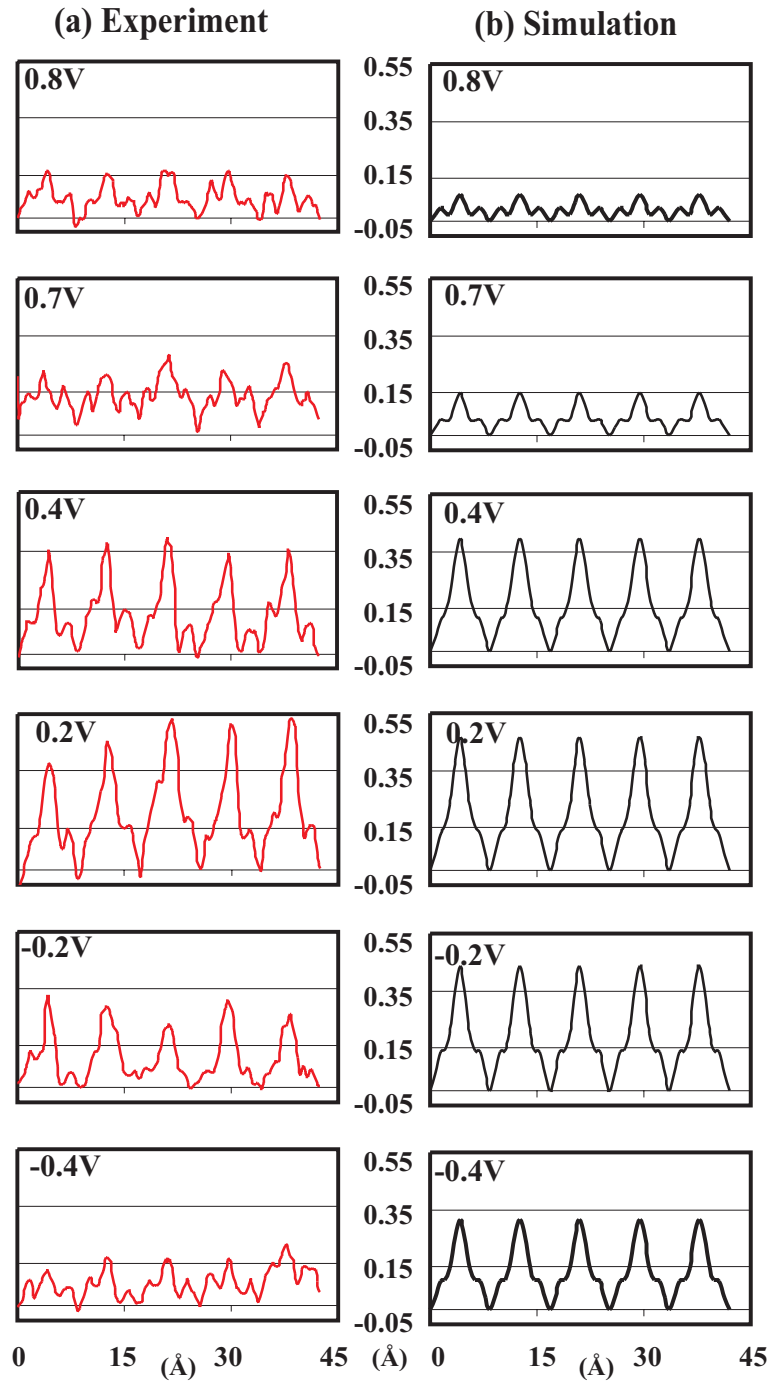
newpage

FIG. 7. (a) Experimental CC height profiles of the STM data obtained along the [101] surface direction for the different sample bias voltages indicated; (b) Simulated CC height profiles along the [101] surface direction for corresponding sample bias voltages.
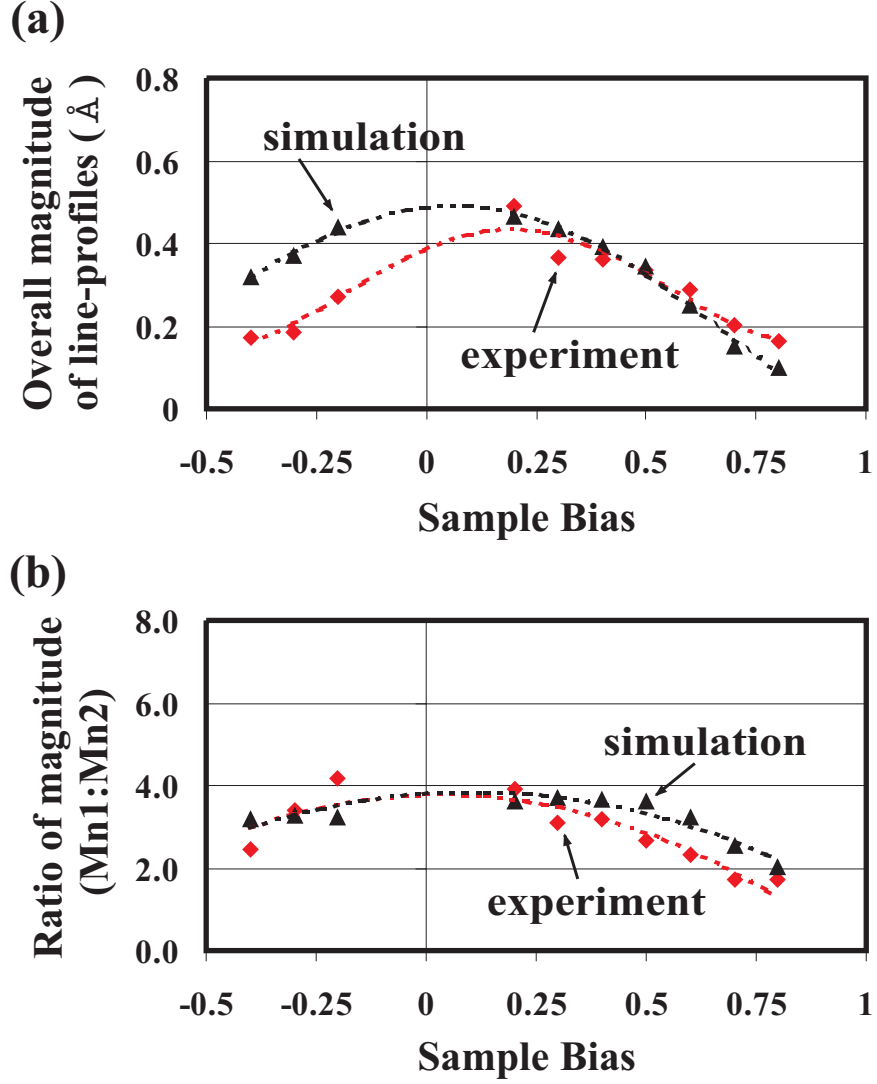
FIG. 8. (a) Experimental and simulated corrugation amplitudes, $A_{Mn1,exp}$ (diamonds) and $A_{Mn1,sim}$ (triangles), as a function of sample bias voltage; (b) Ratio of Mn1 to Mn2 corrugation amplitudes for both experiment (diamonds) and simulation (triangles) as a function of sample bias. Trend lines for experiment and simulation are indicated by the dashed lines in both (a) and (b).